J Mater Sci: Mater Electron (2026) 37:372

Effect of excessive thickness on microwave absorption performance in $SrFe_{12}O_{19}$/MWCNT composite materials

Ismayadi Ismail[1,*], Rabaah Syahidah Azis[1,2], Puteri Noorzulaikha Mohd Badrizazli[2], and Mohd Khairil Adzhar Mahmood[3]

[1] *Nanomaterial Synthesis and Characterization Laboratory, Institute of Nanoscience and Nanotechnology (ION2), Universiti Putra Malaysia, 43400 Serdang, Selangor, Malaysia*
[2] *Department of Physics, Faculty of Science, Universiti Putra Malaysia, 43400 Serdang, Selangor, Malaysia*
[3] *Microwave Research Institute, Universiti Teknologi MARA (UiTM), 40450 Shah Alam, Selangor Darul Ehsan, Malaysia*

Received: 6 November 2025
Accepted: 2 February 2026

ABSTRACT

This research examines the influence of excessive material thickness on the microwave absorption efficiency of $SrFe_{12}O_{19}$/MWCNT composite materials, emphasizing their electromagnetic properties within the X-band frequency range (8–12 GHz). The synthesis of the composites was performed using high-energy ball milling (HEBM) and chemical vapor deposition (CVD) techniques, followed by comprehensive characterization of their structural, magnetic, and dielectric attributes. The study identified an optimal material thickness of 4 mm, achieving maximum reflection loss (RL) efficiency, with a minimum RL of − 1.16 dB was observed for Sample S3 at a thickness of 6 mm in the X-band (8–12 GHz) in MWCNT-integrated samples. Incremental increases in thickness beyond 4 mm led to reductions in microwave absorption performance, attributed to absorption peak shifts and reduced electromagnetic matching efficiency. Magnetic characterization revealed significant reductions in saturation magnetization (M_s) and retentivity (M_r) in MWCNT-incorporated samples due to structural alterations, while coercivity (H_c) was primarily influenced by grain size and synthesis parameters. Dielectric analysis highlighted the enhancement of dielectric loss (ε'') driven by interfacial polarization and MWCNT distribution, particularly at lower frequencies. These findings show the critical interdependence of material thickness, magnetic, and dielectric properties in optimizing radar-absorbing materials, offering key insights for the advancement of composite nanostructures in electromagnetic wave absorption applications.

Address correspondence to E-mail: ismayadi@upm.edu.my

https://doi.org/10.1007/s10854-026-16760-9
Published online: 12 February 2026

1 Introduction

Microwave absorption represents a pivotal area of research in materials science, particularly within the context of electromagnetic applications. The interaction of electromagnetic (EM) waves, including microwaves, with materials involves reflection, transmission, and absorption processes, which collectively govern energy dissipation and attenuation behavior [1–3]. Magnetic materials, in particular, exhibit distinctive microwave absorption characteristics, where enhanced magnetic responses are often associated with improved absorption efficiency [4, 5]. These properties are critically important for modern microwave communication technologies, including mobile communication systems and satellite networks, where effective suppression of unwanted electromagnetic interference is essential for reliable signal transmission [6]. Among the various design parameters, material thickness plays a decisive role in determining wave interference conditions, impedance matching, and attenuation performance, yet its influence beyond conventional coating dimensions remains insufficiently explored.

The interaction of microwaves with materials is fundamentally governed by electromagnetic theory, as described by Maxwell's equations, and is intrinsically dependent on electrodynamic parameters such as complex permittivity (ε), permeability (μ), and electrical conductivity. Within this framework, ferrites have emerged as important functional materials due to their favorable electromagnetic characteristics and wide range of technological applications. Among them, strontium hexaferrite ($SrFe_{12}O_{19}$) has attracted considerable attention owing to its high saturation magnetization, high Curie temperature, chemical stability, cost-effective synthesis, and environmentally benign nature [7–9]. These attributes make $SrFe_{12}O_{19}$ a promising candidate for electromagnetic wave-absorbing applications, including radar-absorbing materials [10, 11]. However, despite its advantageous magnetic properties, pristine $SrFe_{12}O_{19}$ typically exhibits limited microwave attenuation, primarily due to insufficient dielectric loss and impedance mismatch.

Recent studies further indicate that state-of-the-art ferrite/spinel-oxide absorber design increasingly relies on synergistic regulation of dielectric–magnetic losses and heterointerface engineering to improve impedance matching and attenuation at millimeter-scale thickness. For instance, a bimetallic MOF-derived $Cu/C@Fe_3O_4$ system was reported to achieve RL_{min} = − 44.00 dB at 1.65 mm with a 5.84 GHz effective absorption bandwidth at 1.70 mm, demonstrating that tailored interfaces and coupled loss mechanisms can yield strong absorption at relatively thin matching thicknesses [12]. In parallel, rare-earth-oxide-regulated interfacial engineering in $NiCo_2O_4/CeO_2$ composites was shown to enhance dielectric response and facilitate impedance matching, delivering a 6.37 GHz effective absorption bandwidth at 2 mm and RL_{min} ≈ − 60 dB at ~2.20 mm, with polarization loss reported as the dominant contribution within the absorption band [13].

To overcome these limitations, several strategies have been widely explored to enhance the microwave absorption performance of $SrFe_{12}O_{19}$-based materials. The first approach involves substituting iron ions with selected transition elements, which has been shown to reduce coercivity and shift reflection loss (RL) peaks toward lower, more application-relevant frequency ranges [14]. The second strategy focuses on optimizing microstructural and morphological features, including particle size, shape, and distribution, to improve both magnetic and dielectric responses [15, 16]. Although these approaches can enhance absorption efficiency to some extent, the inherently limited dielectric loss of ferrite-based systems remains a significant challenge. As a result, reliance on either magnetic or dielectric loss mechanisms alone often leads to suboptimal electromagnetic wave attenuation, while impedance mismatch further restricts effective energy dissipation [17].

In this context, the incorporation of multi-walled carbon nanotubes (MWCNTs) into $SrFe_{12}O_{19}$-based composites has emerged as an effective strategy to enhance dielectric loss and improve impedance matching. MWCNTs are widely recognized for their excellent electrical conductivity and mechanical robustness, making them suitable dielectric fillers for hybrid microwave-absorbing systems. By integrating MWCNTs with $SrFe_{12}O_{19}$, a synergistic combination of magnetic and dielectric components can be achieved, enabling enhanced microwave absorption performance. For example, Ref. [18]] reported the fabrication of Mn–Cu–Zr-substituted $SrFe_{12}O_{19}$/MWCNT nanocomposites, where the incorporation of 7 wt% MWCNTs resulted in a broad absorption bandwidth of approximately 6 GHz and enhanced RL characteristics, despite reductions in saturation and remanent magnetization.

Consistent with these findings, Ref. [19] investigated $SrFe_{12}O_{19}$ nanoparticles and $SrFe_{12}O_{19}$/MWCNT nanocomposites synthesized via a sol–gel route, demonstrating improved microwave absorption performance for the nanocomposites compared to the individual ferrite nanoparticles. Similarly, Ref. [20] reported that Zn–Sn-substituted strontium ferrite films anchored onto MWCNT surfaces exhibited markedly enhanced microwave absorption characteristics relative to their ferrite-only counterparts. Despite these advances, the majority of reported studies have primarily focused on compositional optimization and absorption bandwidth enhancement, while the influence of material thickness, particularly beyond conventional absorber dimensions, has received limited attention.

Although practical microwave-absorbing coatings are typically designed with thicknesses of approximately 1 mm, the present study does not aim to propose a coating-ready configuration. Instead, it systematically investigates the electromagnetic response of $SrFe_{12}O_{19}$/MWCNT composites at excessive thicknesses ranging from 4 to 6 mm, with the objective of elucidating attenuation trends, interference effects, and performance degradation beyond the commonly studied thickness regime. Previous work, as discussed in Ref. [21], has addressed absorption behavior within the 1–3 mm thickness range; notably, the 2 mm X-band performance of the Sr-hexaferrite/CNT system was reported in Ref. [21], where the best 2 mm case (S5) achieved RL_{min} − 16.5 dB at 8.5 GHz (0.3 GHz bandwidth) and − 10.7 dB at 10.8 GHz (0.1 GHz bandwidth). However, a clear research gap persists regarding the role of greater thicknesses in governing RL behavior and microwave absorption efficiency in hybrid $SrFe_{12}O_{19}$/MWCNT systems.

Accordingly, this study seeks to address this gap by examining how the structural, morphological, and microwave absorption properties of $SrFe_{12}O_{19}$/MWCNT composites vary with material thicknesses of 4 mm, 5 mm, and 6 mm. It is important to clarify that the complex permittivity and permeability were analyzed to understand these effects. The $SrFe_{12}O_{19}$ nanoparticles were synthesized via high-energy ball milling (HEBM), followed by the incorporation of MWCNTs using chemical vapour deposition (CVD). Through systematic thickness-dependent investigations, this work provides deeper insights into the role of excessive thickness in microwave absorption behavior and to identify design considerations for optimizing composite-based radar-absorbing materials.

2 Methodology

Strontium hexaferrite ($SrFe_{12}O_{19}$) was synthesized using high-purity raw materials, specifically strontium carbonate ($SrCO_3$) and hematite (Fe_2O_3), each with a purity of 99.8% and sourced from Alfa Aesar. The synthesis process involved the precise blending of $SrCO_3$ and Fe_2O_3 in their stoichiometric proportions, enabling the formation of $SrFe_{12}O_{19}$ according to the following reaction:

$$SrCO_3(s) + Fe_2O_3(s) \rightarrow SrFe_{12}O_{19}(s) + CO_2(g). \quad (1)$$

2.1 Raw material weighing for $SrCO_3$ and Fe_2O_3

In order to attain the desired composition, the objective was to achieve a total mass of 10 g for the strontium hexaferrite. This involved the allocation of 1.71 g to $SrCO_3$ and 8.29 g to Fe_2O_3, as outlined in Table 1.

The raw mixed powders were subjected to HEBM, designated as Sample 1 (S1). The process employed a ball-to-powder ratio (BPR) of 5:1 and was carried out for 10 h at room temperature using a SPEX800D milling machine. During milling, the powders were carefully mixed, producing a brown-reddish material that was loaded into vials along with metal balls. To prevent powder aggregation and enhance milling efficiency, intermittent pauses were implemented, allowing for manual scraping of the vial contents. Following the milling process, the powders were further homogenized using a ground mortar for 15 min to ensure uniform consistency.

After the HEBM process, the powders were subjected to sintering at 900 °C for 10 h with a controlled heating rate of 3 °C per second. This process induced a color change in the powders from brown-reddish to brownish-black. The sintered product, designated as Sample 2 (S2), was then divided into two portions. One portion underwent an additional 10 h of HEBM under identical milling conditions, resulting in

Table 1 Mass of compound utilized for milling (10 g)

Chemical name	Compound formula	Molecular mass (g/mol)	Mass (g)
Strontium carbonate	$SrCO_3$	147.629	1.71
Hematite	Fe_2O_3	718.146	8.29
		Total	10

Sample 3 (S3). Throughout this secondary milling, the powders were thoroughly mixed at regular intervals to ensure homogeneity. Both S2 and S3 were subsequently utilized as carbon sources for the subsequent stages of the synthesis process.

2.2 Hybridization of $SrFe_{12}O_{19}$ with MWCNTs via CVD

To achieve the hybridization of $SrFe_{12}O_{19}$ with MWCNTs, Samples S2 and S3 were utilized as catalysts for carbon nanotube synthesis via the CVD technique. The prepared samples were evenly distributed on a ceramic boat, which was subsequently placed inside a tube furnace. To eliminate oxygen from the system, argon gas was introduced, and the furnace was gradually heated to 800 °C. Ethanol (C_2H_5OH) was vaporized, providing the hydrocarbon source for the CVD process. After maintaining the temperature at 800 °C for 20 min, the furnace was cooled to room temperature. The resulting MWCNTs were collected and designated as Samples S4 and S5. Further details of the experimental procedure are available in Ref. [21].

2.3 Material characterization and electromagnetic wave absorption performance

X-ray diffraction (XRD) (Philips X'pert Diffractometer Model 7602 in a 2θ range of 20–80°) analysis was conducted to determine the composition, crystalline structure, and phase purity of the samples. The RL, permeability, and dielectric properties within the X-band frequency range were evaluated using a PNA network analyzer N5227A via transmission reflection line method (TRL) in the 8–12 GHz (X-band). It is important to clarify that the complex permittivity and permeability retrieved using the waveguide TRL method representing intrinsic, normalized material properties and are independent of sample thickness. In contrast, the RL is not an intrinsic parameter but a structure-dependent quantity governed by transmission-line theory, where absorber thickness directly influences impedance matching and interference conditions. Therefore, variations in RL with thickness observed in this study originate from geometric and wave-propagation effects rather than changes in ε_r or μ_r. Furthermore, the magnetic properties, including saturation magnetization, retentivity, and coercivity, were characterized through measurements performed with a Vibrating Sample Magnetometer (VSM) (Lakeshore Model 7404) at room temperature.

2.4 Sample preparation for microwave measurements and characterization

For microwave measurements, solid pellets were fabricated using an epoxy resin–hardener system mixed at a mass ratio of 3:1. For samples S2 and S3, which had not undergone the CVD process, the optimal filler content was determined to be 60 wt% [22]. In contrast, for Samples S4 and S5, which were subjected to the CVD process, the filler content was set at 6 wt%. These composite mixtures were carefully molded into sample holders of varying thicknesses (4 mm, 5 mm, and 6 mm) to enable measurements within the X-band frequency range (8–12 GHz).

3 Results and discussion

3.1 Microstructural analysis of MWCNTs using unmilled and milled $SrFe_{12}O_{19}$

Microstructural analysis of the MWCNTs in Samples S4 and S5 provided valuable insights into their growth and characteristics. Figure 1a illustrates the microstructure of Sample S4, which was catalyzed by unmilled $SrFe_{12}O_{19}$, while Fig. 1b depicts the microstructure of Sample S5, catalyzed by milled $SrFe_{12}O_{19}$. A notable difference in MWCNT diameters was observed between the two samples, attributed to the influence of the catalyst size during the CVD process [23]. The microstructural analysis revealed that the MWCNTs in Sample S4 had an average diameter of approximately 215 nm, whereas those in Sample S5 exhibited a smaller average diameter of around 93 nm. This variation highlights the critical influence of catalyst size on growth kinetics, which ultimately determines the dimensions of the MWCNTs [24]. Additionally, the presence of catalyst particles at the tips of the MWCNTs provided evidence of a tip-growth mechanism, indicating that the MWCNTs predominantly grew from their tips, resulting in hollow tubes with well-defined layers. A more detailed and comprehensive microstructural analysis has been documented in Ref. [21]. Although the contrast between $SrFe_{12}O_{19}$ particles and MWCNTs is not distinctly resolved in the SEM images due to their nanoscale intergrowth and surface coverage, the successful hybridization is

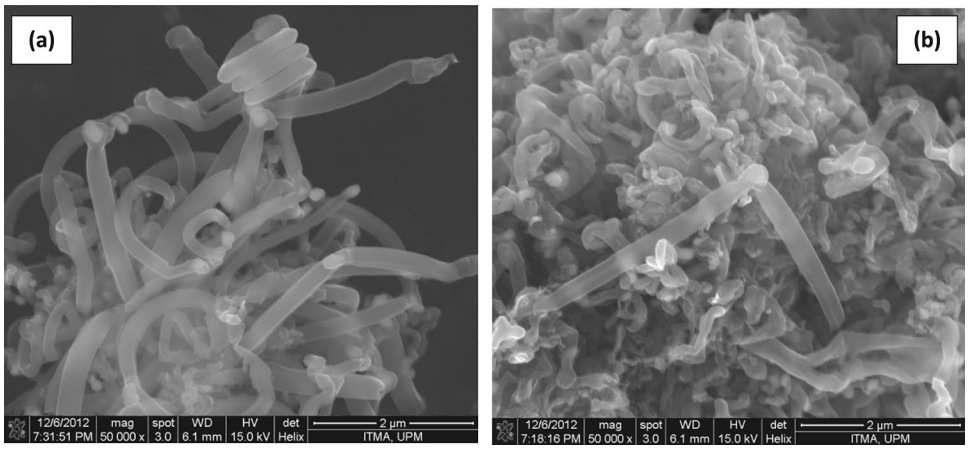

Fig. 1 FeSEM images depict the microstructure of **a** the S4 sample, catalyzed by $SrFe_{12}O_{19}$ without milling and **b** the S5 sample, catalyzed by $SrFe_{12}O_{19}$ after milling

independently confirmed by XRD phase analysis and the corresponding changes in magnetic and dielectric responses.

The diameter of MWCNTs significantly influenced their electromagnetic properties, including RL. RL, which characterizes the absorption or reflection of electromagnetic energy when waves interact with a material, was governed by the complex relationship between MWCNT diameter and their resonant behavior. The distinctive electromagnetic properties of MWCNTs arose from their cylindrical structure and the quantization of electronic states on their surfaces. These characteristics were determined by factors such as the nanotube's diameter, length, and carbon atom arrangement. Electromagnetic wave interactions induced electron oscillations along the surface of the nanotubes, generating surface currents that shaped their overall electromagnetic behavior [25].

The frequency-dependent behavior of complex permittivity (ε) and permeability (μ) governs the RL of materials. In the case of MWCNTs, their diameter plays a critical role in determining resonant frequencies, which directly influence ε and μ. These resonant frequencies are dictated by the nanotubes' dimensions and electronic structure, corresponding to distinct electromagnetic modes such as radial and axial modes. Resonance occurs when the MWCNT diameter aligns with the wavelength of the incident electromagnetic waves, enhancing energy absorption, reducing reflection, and increasing RL. Notably, the resonant frequencies depend on the dimensions, length, and surrounding electromagnetic environment of the nanotubes. MWCNTs with larger diameters exhibit resonances at lower frequencies due to elongated axial modes, while smaller-diameter MWCNTs resonate at higher frequencies [26]. The ability to manipulate the diameter of MWCNTs enables the customization of their resonant behavior, thereby optimizing RL for targeted frequency ranges. The resonant frequencies of MWCNTs can be approximated using the equation governing the axial modes of a cylindrical resonator:

$$F_{\mathrm{n}} = \frac{v}{2L}.n, \tag{2}$$

where F_{n} is the resonant frequency of the n-th mode, v is the phase velocity of the wave (typically the speed of light in vacuum), L is the length of the resonator (in this case, the length of the MWCNT), and n is the mode number. For larger-diameter MWCNTs, the longer axial modes (corresponding to higher mode numbers, n) result in resonances occurring at lower frequencies. Conversely, smaller-diameter MWCNTs exhibit resonances at higher frequencies due to the shorter axial modes. Adjusting the diameter (D) of the MWCNTs effectively modifies the resonator length (L), thereby influencing the resonant frequencies.

3.2 Phase analysis and crystallographic structure of $SrFe_{12}O_{19}$ and $SrFe_{12}O_{19}$/MWCNTs nanocomposites

The phase formation during synthesis was validated through XRD analysis. The XRD pattern of the S1 sample, shown in Fig. 2, indicated the presence of initial materials, such as Fe_2O_3 and $SrCO_3$, identified using their respective ICSD reference codes (98-004-6403 for Fe_2O_3 and 98-004-6256 for $SrCO_3$). While the peaks were consistent with the hexagonal phase of Fe_2O_3, specific peaks at 25.25° corresponded to the (111) plane of the $SrCO_3$ phase. The XRD patterns for S2

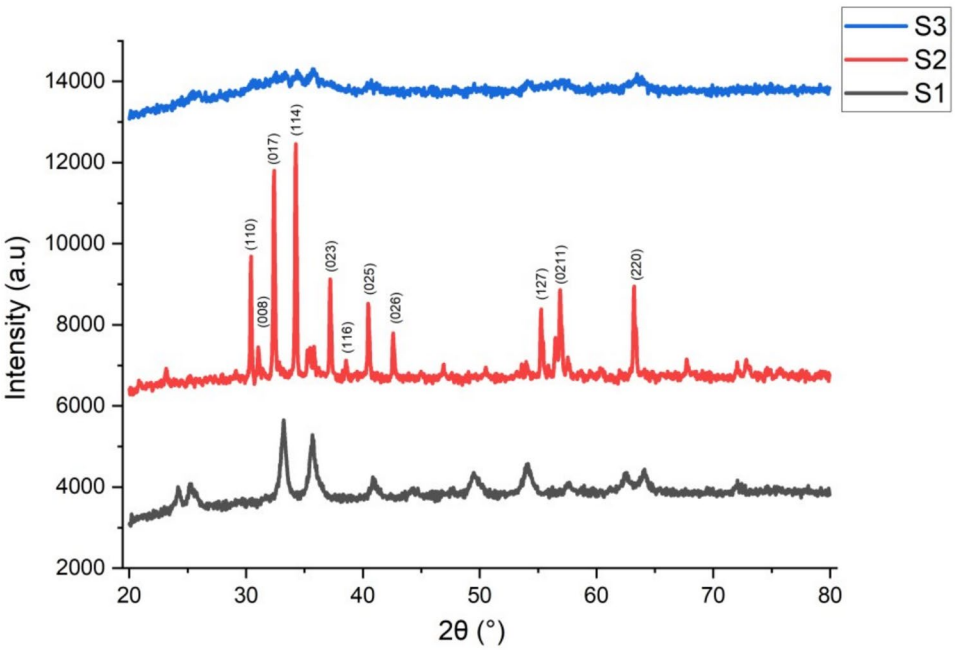

Fig. 2 XRD patterns of S1, S2, and S3

and S3, after sintering at 900 °C and subsequent 10-h milling for S3, demonstrated the dominant formation of the hexagonal M-type phase. S2 exhibited sharp diffraction peaks, indicative of improved crystallinity, with peaks at 2θ values of 31.04°, 34.23°, 38.55°, and 63.21°, corresponding to the (008), (114), (116), and (220) planes, consistent with the standard pattern for M-type hexaferrite. In contrast, the XRD pattern for S3 revealed the emergence of additional phases due to prolonged milling, resulting in reduced crystallite size, increased lattice parameters, and elevated strain. The pattern also displayed multiple defect-related features, likely arising from significant structural deformation during the extended milling process. The significantly larger FWHM observed for Sample S3 is attributed to the prolonged HEBM process, which introduced severe lattice strain, crystallite fragmentation, and a high density of structural defects, collectively resulting in pronounced peak broadening.

The diffracted peaks for Samples S4 and S5 (Fig. 3) reveal distinct signatures corresponding to MWCNTs at the (002) and (004) planes. The (002) peak, in particular, is significant as it represents the interlayer spacing within the graphitic structure, a defining characteristic of MWCNTs. The presence of these peaks confirms the successful synthesis of MWCNTs in both samples, with the (002) peak appearing more pronounced in Sample S5 compared to Sample S4. This observation is consistent with findings by Inagaki et al., who reported that the intensity ratios of the (002) to (004) diffraction lines can provide valuable insights into the structural properties of carbon-based materials. [27]. The (004) peak, being weaker, aligns with the typical behavior of graphitic materials, where the (002) peak predominates due to its fundamental role in defining the crystal structure [28]. The increased intensity of the (002) peak in Sample S5 compared to Sample S4 suggests a reduction in particle size, a phenomenon well documented in the literature. For instance, Cao et al. reported that a higher intensity of the (002) peak is often associated with smaller particle dimensions, leading to a more compact arrangement of carbon nanotubes (CNTs) [28]. Additionally, the upward shift of the (002) peak in Sample S5 indicates not only changes in particle size but also potential alterations in the material's crystallinity. This observation is consistent with findings by Zhao et al., who noted that shifts in diffraction peaks often reflect modifications in the structural properties of carbon-based materials [29]. Moreover, the upward shift of the (002) peak in S5 signifies not only a change in particle size but also a potential alteration in the crystallinity of the material. This is corroborated by the findings of Zhao et al., who observed that changes in the diffraction peaks can reflect modifications in the structural properties of carbon-based materials [30]. These structural changes

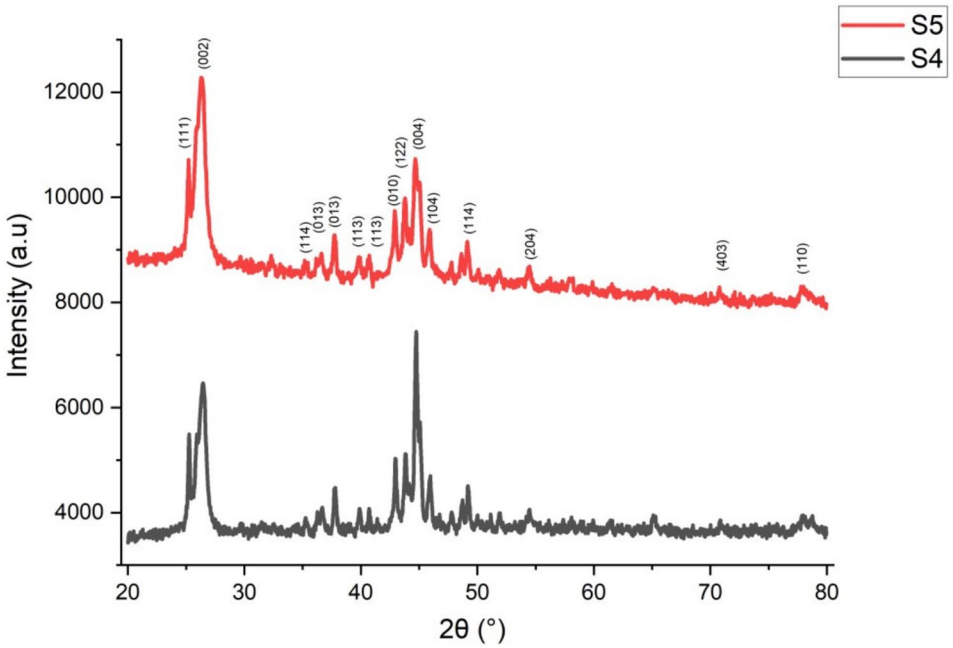

Fig. 3 XRD patterns of S4 and S5

have significant implications, as they can directly influence the electrical and mechanical properties of the synthesized MWCNTs, showing the critical relationship between microstructural characteristics and functional performance.

The Scherrer equation was employed to estimate the nanocrystalline particle dimensions within the sample, utilizing the full width at half maximum (FWHM) values derived from the XRD pattern. The equation is expressed as

$$L = K\lambda/\beta * \cos\theta, \quad (3)$$

where L is the crystallite size, K is the Scherrer constant (a shape factor typically around 0.9), λ is the X-ray wavelength, β is the FWHM of the diffraction peak, and θ is the diffraction angle.

Table 2 presents the FWHM and crystallite size values for each sample, with Sample S3 exhibiting the highest FWHM value, indicative of the smallest crystallite size. The FWHM represents the width of the diffraction peak at half of its maximum intensity. According to the Scherrer equation, an increase in the FWHM corresponds to a reduction in crystallite size, and vice versa.

The trend observed in Sample S3 can be attributed to the extended milling duration employed during the preparation of the nanocomposite. The milling process involves repeated deformation, crushing, and grinding of particles, leading to a significant reduction in grain size [31]. For Sample S3, the extended milling duration resulted in more pronounced deformation and fragmentation of particles, leading to a reduction in crystallite size. This increased deformation and fragmentation created additional active sites and defects on the surface of the catalyst, which could act as nucleation sites for the growth of MWCNTs. Consequently, this may result in a higher density of MWCNTs, influencing their diameter and length.

Furthermore, the fragmentation of particles introduced additional carbon atoms and reactive species into the reaction environment, which likely contributed to the catalytic growth of MWCNTs. The smaller crystallite sizes, a direct outcome of the intensified

Table 2 XRD parameter of indices Miller *hkl*, 2θ, full width of half maximum (FWHM), and the crystallite size of $SrFe_{12}O_{19}$/MWCNTs composites samples

Samples	(*hkl*)	2θ (°)	FWHM (radian)	Crystallite size (nm)
S1	104	33.177	0.537	170
S2	114	34.230	0.128	1062
S3	011	32.490	3.208	26
S4	002	26.406	0.621	143
S5	002	26.299	0.671	131

deformation and fragmentation, enhanced the catalytic activity and nucleation process. This effect potentially altered the structural characteristics of the resulting MWCNTs, including their growth dynamics and final properties [31].

The size and morphology of MWCNTs are crucial parameters, as smaller crystallite sizes can result in MWCNTs with modified electronic and electromagnetic properties, thereby influencing their interaction with electromagnetic waves [32]. The morphology of MWCNTs plays a significant role in determining their resonant behavior and absorption capabilities. Furthermore, the presence of defects and the increased surface area arising from fragmentation introduce additional mechanisms for electromagnetic energy absorption. These structural and morphological changes can substantially enhance the efficiency of microwave absorption.

3.3 Hysteresis loops and magnetic properties of $SrFe_{12}O_{19}$/MWCNTs nanocomposites

The magnetization behavior of the $SrFe_{12}O_{19}$/MWCNT composites synthesized from different samples was analyzed (Fig. 4), revealing hysteresis loops and key magnetic parameters such as saturation magnetization (M_s), retentivity (M_r), and coercivity (H_c). These parameters provide insight into the magnetic characteristics of the composites, with detailed values summarized in Table 3. Among the samples, S2, subjected

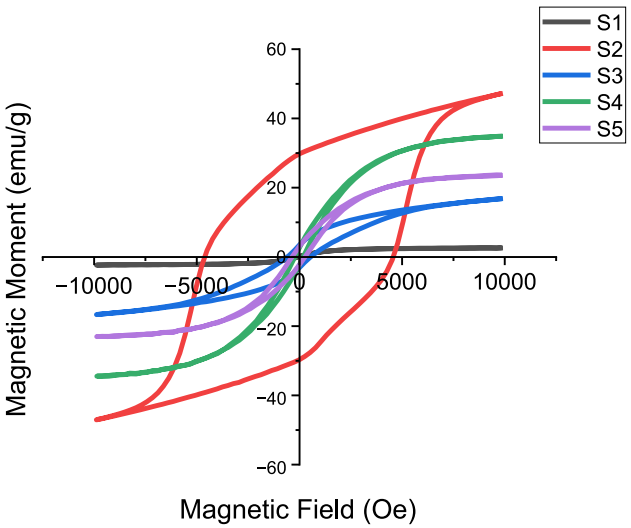

Fig. 4 Magnetization curves of $SrFe_{12}O_{19}$ and $SrFe_{12}O_{19}$/MWCNTs nanocomposites

Table 3 Magnetic characteristics of each sample

Samples	M_s (emu/g)	M_r (emu/g)	H_c (Oe)
S1	2.509	$71.439E^{-3}$	47.08
S2	47.158	29.727	4586.70
S3	16.750	3.2756	568.95
S4	34.673	2.4847	205.81
S5	23.368	2.6733	317.04

to 10 h of milling followed by sintering at 900 °C, exhibited the highest M_s value of 47.158 emu/g. This increase compared to S1 can be attributed to the sintering process, which enhanced grain size and reduced porosity, thereby improving magnetic performance. In contrast, S1 displayed a smooth magnetization curve characteristic of a hard magnet, indicative of high-phase purity and well-defined crystallinity.

Sintering involves subjecting powdered $SrFe_{12}O_{19}$ particles to elevated temperatures, typically near or slightly below their melting point, for a defined period. At these elevated temperatures, diffusion-driven bonding occurs between particles as increased thermal energy enhances atomic mobility, facilitating atom migration across particle boundaries. This process leads to particle fusion, resulting in the formation of a solid, compact, and interconnected structure. During this fusion, the dimensions of individual particles expand due to atom migration and rearrangement. The boundaries between adjacent particles diminish, promoting the formation of larger grain sizes within the material. The growth of these grains supports the development of additional magnetic domains, which, in turn, enhances the magnetization levels of the material [33].

In the early stages of sintering, incomplete particle fusion can result in higher porosity. However, as the sintering process progresses and particle boundaries dissolve, pore dimensions decrease, leading to reduced porosity. This densification enhances the material's magnetic properties by restricting magnetic domain wall movement and promoting greater magnetic coherence. The simultaneous enlargement of grain size and reduction in porosity during sintering contribute significantly to the improvement of the material's magnetic characteristics. Larger grain sizes support the formation of more magnetic domains, leading to higher saturation magnetization (M_s). Furthermore, a denser and more uniform structure, characterized by reduced porosity, enhances

magnetic coherence, thereby increasing retentivity (M_r) and coercivity (H_c). These changes in grain size and porosity critically influence the alignment and stability of magnetic domains, which are essential determinants of the material's overall magnetic behavior [34].

These phenomena can be correlated with the Curie–Weiss law elucidates the magnetic susceptibility (χ) of a material concerning temperature (T) and offers valuable insights into the material's magnetic behavior [33].

The Curie–Weiss law is represented by the equation:

$$\chi = C/(T - \theta), \tag{4}$$

where χ is the magnetic susceptibility, C is the Curie constant (a material-specific constant), T is the temperature in Kelvin, and θ is the Curie temperature, which is a material-specific parameter.

Sintering, through its effects on grain size and porosity, significantly influences magnetic coherence and the strength of magnetic interactions among atoms or ions in the material. The increase in grain size and reduction in porosity enhance magnetic coherence, which in turn raises the Curie temperature (θ) of the material. A higher Curie temperature indicates improved magnetic stability at elevated temperatures. Additionally, the sintering process impacts the Curie constant (C) by altering the arrangement and interactions of atoms or ions within the material's microstructure. The Curie constant, which is directly related to the strength of magnetic interactions, can be modified by these structural changes, thereby affecting the material's magnetic susceptibility. These interconnected effects of sintering on grain size, porosity, and microstructural arrangement play a critical role in determining the material's overall magnetic performance [33].

In contrast, Sample S3 demonstrated a lower saturation magnetization (M_s), which can be attributed to the additional 10 h of HEBM. This extended milling duration resulted in a significant reduction in grain size. During the HEBM process, powder particles are subjected to intense mechanical forces and repeated collisions with the milling balls, leading to plastic deformation and fragmentation. As milling progresses, the particles undergo increasingly pronounced deformation and fragmentation, contributing to a steady decrease in their average grain size. This reduction occurs due to the accumulation of defects and dislocations within the material, which serve as nucleation sites for the formation of grain boundaries. Consequently, new, smaller grains are formed, refining the microstructure of the material. This continuous cycle of deformation and fragmentation effectively reduces the average grain size, which explains the observed decrease in M_s for Sample S3 [31]. The grain size reduction observed during HEBM can be interpreted through the Hall–Petch equation, which establishes the relationship between grain size and yield strength in polycrystalline materials:

$$\sigma_y = \sigma_o + K_y.d^{-1/2}, \tag{5}$$

where σ_y is the yield strength of the material, σ_o is the initial (undeformed) yield strength, K_y is the Hall–Petch constant, which depends on material properties, and d is the average grain size of the material. The Hall–Petch equation shows that a decrease in grain size (d) corresponds to an increase in yield strength (σ_y) [35]. The relationship described by the Hall–Petch equation arises from the increased presence of grain boundaries in materials with smaller grains. These grain boundaries act as barriers to dislocation motion, impeding plastic deformation, thereby enhancing the material's strength. During HEBM, the grain size (d) of the material decreases due to the repeated deformation and fragmentation of particles. According to the Hall–Petch equation, this reduction in grain size leads to an increase in yield strength.

This increase in strength is often accompanied by higher hardness and improved mechanical properties, attributes commonly observed in materials with reduced grain size as a result of mechanical processing such as HEBM. These enhancements are directly linked to the refined microstructure and the greater resistance to deformation provided by the smaller grains and their associated grain boundaries.

Prolonged milling during HEBM introduces structural irregularities such as grain boundaries and dislocations, as previously noted. These anomalies disrupt the long-range magnetic order within the material, affecting the alignment of magnetic domains. This disruption can result in misalignment or reduced alignment of magnetic moments across different domains, leading to a decrease in saturation magnetization (M_s). Additionally, the reduction in grain size associated with extended milling increases the density of grain boundaries. The higher density of grain boundaries

further impedes the overall magnetic coherence by interrupting the continuous magnetic structure. As a result, the material exhibits a lower M_s, reflecting the cumulative effects of diminished magnetic alignment and increased structural interruptions [33].

For Samples S4 and S5, the saturation magnetization (M_s) values were comparatively lower than those reported in the literature, as shown in Table 3. This reduction in magnetic moment can be attributed to structural modifications occurring on the surface of the ferrites. Factors contributing to this phenomenon include the small size and surface imperfections of the ferrite crystallites, as well as strain arising from the interaction between the surfaces of the ferrite nanoparticles and the MWCNTs. These structural and interfacial effects likely influence the overall magnetic properties of the composite material.

Sample S3, which underwent a longer milling duration, was expected to exhibit a lower coercivity (H_c) compared to Sample S2. This reduction in magnetic parameters is likely due to the pronounced amorphization resulting from extended milling [36]. Additionally, samples incorporating MWCNTs displayed reduced H_c values, as the magnetic properties of the composite were predominantly governed by the $SrFe_{12}O_{19}$ particles. This behavior can be attributed to the structural influence on coercive force, which is more dependent on the material's microstructure than its intrinsic composition. Consequently, this led to the formation of a single-domain structure in the strontium ferrite.

3.4 Reflection loss assessment for $SrFe_{12}O_{19}$/MWCNTs nanocomposites

This study aims to examine the microwave absorption properties of $SrFe_{12}O_{19}$ combined with MWCNTs within the X-band frequency range, particularly focusing on samples with varying thicknesses. The analysis, conducted using a Vector Network Analyzer (VNA), identifies the frequencies at which RL occurs in the samples. The results, as shown in Fig. 5, present the RL values for samples with thicknesses of 4 mm, 5 mm, and 6 mm. In this context, "loss" refers to lower RL, signifying enhanced absorption and highlighting the material's potential as an effective microwave-absorbing medium.

Reflection loss (RL) is a key parameter in evaluating the efficiency of microwave-absorbing materials, as it indicates the material's ability to attenuate

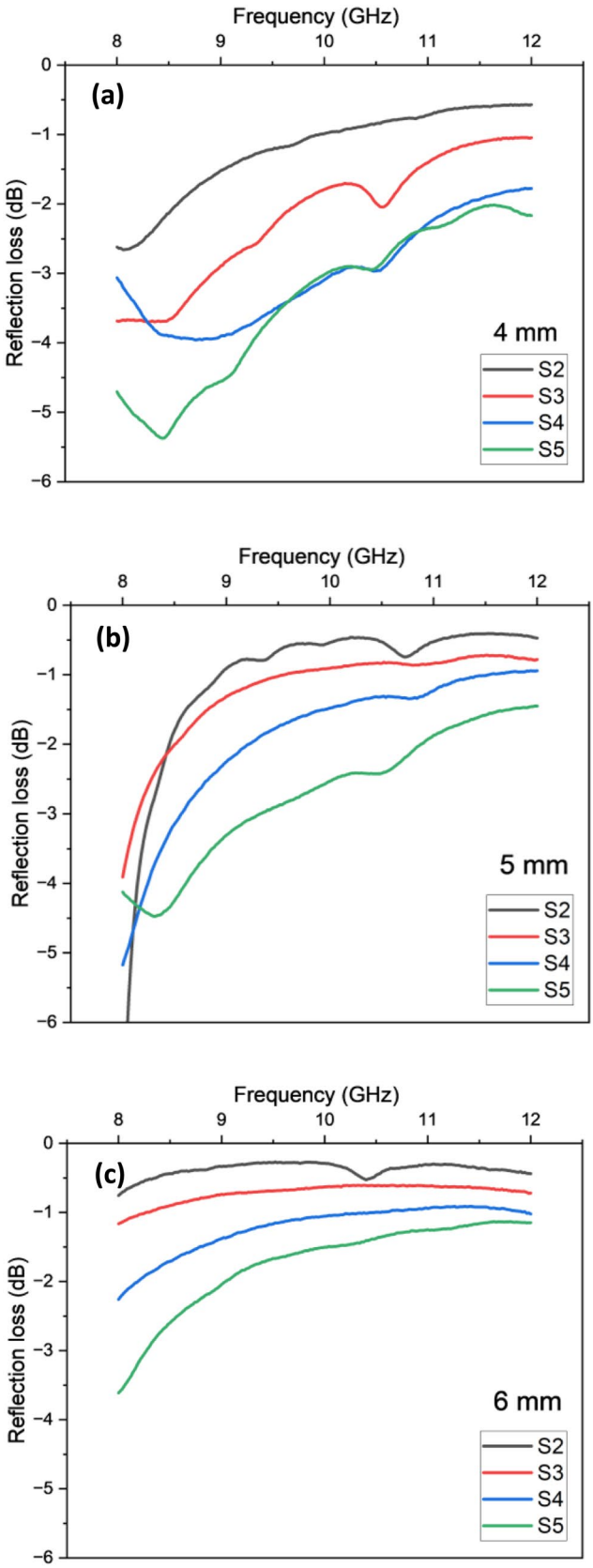

Fig. 5 VNA graph of **a** 4 mm, **b** 5 mm, and **c** 6 mm for all samples

electromagnetic waves. The relationship between sample thickness and RL is well established in the literature. For example, Co et al. reported that RL is strongly influenced by sample thickness, with variations in thickness altering both the intensity and the position of RL peaks. This demonstrates the critical role of sample thickness in optimizing the material's performance as a microwave absorber [37]. This is consistent with the findings of Ref. [38] who also emphasize that the electromagnetic wave absorption efficiency is expressed through RL, which is dependent on the thickness of the absorbing materials [38].

The primary objective of this study is to investigate the microwave absorption properties of $SrFe_{12}O_{19}$/MWCNT composites with varying thicknesses in the X-band frequency range. Table 4 presents the minimum RL values observed at specific frequencies for each sample thickness. Previous research, as reported in Ref. [21], showed an increase in thickness from 1 to 3 mm led to an increase in RL. However, based on the findings of this current study, it is evident that using a thickness greater than 4 mm results in lower RL.

The trend in minimum RL observed in the samples, as illustrated in Fig. 5, shows an initial increase from a thickness of 4 to 5 mm, followed by a decrease at 6 mm. This indicates that a thickness of 5 mm is optimal for achieving superior microwave absorption (for $SrFe_{12}O_{19}$/MWCNT at X-band). This behavior is consistent with the quarter-wavelength principle, which posits that when the thickness of an absorbing material corresponds to an odd multiple of one-quarter of the operating wavelength, destructive interference occurs between the incident and reflected waves, thereby maximizing electromagnetic energy absorption [39]. Dai et al. corroborate that the relationship between minimum RL and thickness aligns with the quarter-wavelength principle, demonstrating that specific thicknesses can significantly enhance the microwave absorption capabilities of materials [39]. Similarly, findings reported in Ref. [40] support this observation, showing that absorption peaks shift with variations in thickness, emphasizing the critical role of optimizing thickness for effective microwave absorption. Their study illustrates that minimum RL values are achieved at specific thicknesses, consistent with the interference effects predicted by the quarter-wavelength theory. Additionally, Luo et al. further validate this principle, demonstrating that RL values are strongly dependent on the absorber thickness, showing that the necessity of selecting appropriate thicknesses to maximize absorption efficiency [41].

Table 4 Frequency and minimum reflection loss for each thickness of each

Samples	Thickness (mm)	Frequency (GHz)	Minimum RL achieved (dB)
S2	4	8.06	− 2.6603
	5	8.00	− 7.6959
	6	8.00	− 0.7559
S3	4	8.30	− 3.6990
	5	8.00	− 3.9085
	6	8.00	− 1.1649
S4	4	8.76	− 3.9588
	5	8.00	− 5.1757
	6	8.00	− 2.2583
S5	4	8.44	− 5.3728
	5	8.30	− 4.4734
	6	8.00	− 3.6135

At a thickness of 6 mm, Sample S3 demonstrated a higher minimum RL of − 1.1649 dB compared to − 0.7559 dB for Sample S2. This variation can be attributed to the extended milling duration for S3, which resulted in smaller particle sizes, as shown in Fig. 1. The correlation between smaller particle sizes and increased surface area, leading to enhanced particle interactions and improved electromagnetic (EM) absorption, is well documented in the literature. The larger surface area of smaller particles facilitates more extensive contact points and interactions, thereby enhancing the material's absorption capabilities. For example, Guo et al. observed that hollow three-dimensional structures in their composites promoted multiple reflections and refractions of electromagnetic waves, significantly improving EM absorption. This improvement was attributed to the increased surface area and the enhanced interaction of the particles, further supporting the relationship between particle size, surface area, and absorption performance [42]. This observation aligns with the established principle that a larger surface area enhances interactions with electromagnetic fields, thereby improving absorption characteristics. Additionally, the mechanism of dipole formation, wherein regions of positive and negative charges are separated within a material, plays a critical role in facilitating these interactions and contributing to electromagnetic (EM) absorption. Cai further elaborates on this phenomenon, highlighting that

the coupling effect between particles in composites can be intensified, resulting in increased electrical conductivity. This enhancement also leads to higher values of the imaginary component of complex permittivity (ε''), particularly at elevated frequencies, thereby bolstering the material's overall absorption performance [43]. These findings indicate that the interactions facilitated by smaller particles not only increase the surface area but also promote the formation of dipoles, which are essential for effective EM absorption. Dai et al. provide further evidence supporting this concept, demonstrating that the surface anisotropy field and coercivity are enhanced in nanostructured materials. These enhancements contribute to improved absorption of electromagnetic waves, reinforcing the critical role of nanoscale structural features in optimizing absorption performance [44]. The increased surface area and the resulting dipole interactions are pivotal in enhancing the electromagnetic wave absorption properties of these materials. Yadav et al. further emphasize that the interaction of electromagnetic waves with electric and magnetic dipoles is fundamental to the absorption process, showing the critical influence of particle size and distribution on overall absorption efficiency [45]. This observation aligns with the principle that smaller particles, owing to their increased surface area, promote enhanced dipole formation and interactions, thereby improving electromagnetic absorption. The underlying mechanism involves the formation of dipoles—regions within a molecule or material where positive and negative charges are spatially separated. This process is governed by the electric susceptibility (χ), which quantifies the material's response to an applied electric field and can be described mathematically as follows:

$$\text{Polarization } (P) = \chi * \text{Electric field } (E), \tag{6}$$

where Polarization (P) represents the dipole moment induced in the material, and Electric Susceptibility (χ) characterizes the material's ability to polarize in response to an external electric field. It quantifies the degree to which charges become separated within the material. Electric Field (E) is the strength of the external electric field applied to the material. When an external electric field (E) is applied to a material with a non-zero electric susceptibility (χ), dipoles are induced within the material. These dipoles, characterized by regions of positive and negative charges separated within the structure, contribute to the material's polarization. A higher electric susceptibility corresponds to stronger induced polarization, enhancing the material's ability to interact with and absorb EM energy. In the context of EM absorption, these dipoles play a crucial role in facilitating the absorption and dissipation of EM energy. The smaller particle size of Sample S3, resulting from its extended milling duration, provides a higher surface area per unit mass compared to Sample S2. This increased surface area creates more interaction sites between particles, leading to the formation of a greater number of dipoles within S3. These abundant dipoles effectively absorb and dissipate EM energy, thereby contributing to the superior EM absorption properties exhibited by S3 relative to S2.

Sample S5 exhibited a greater minimum RL compared to Sample S4, and both S5 and S4 demonstrated higher minimum RL values than S2 and S3. This trend can be attributed to differences in milling duration and the growth of MWCNTs among the samples. The optimal thickness of 4 mm observed for the $SrFe_{12}O_{19}$/MWCNT composites is consistent with previous reports on ferrite–carbon-based absorbers, where effective microwave absorption in the X-band is typically achieved at thicknesses between 2 and 4 mm. Beyond this range, absorption performance generally deteriorates due to impedance mismatch and RL peak shifting. Similar thickness-dependent trends have been reported by Ref. [46], who highlighted that excessive thickness reduces the effectiveness of dielectric loss relative to magnetic loss, and Refs. [47, 48] who demonstrated that increasing thickness beyond the optimal range leads to degraded dielectric behavior and shifted absorption peaks. The relationship between thickness and RL is particularly significant, as increasing the sample thickness reduces the peak minimum RL and shifts it to a lower frequency. This behavior aligns with the findings of Ref. [49], which indicate that reducing thickness enhances RL in composite materials. Furthermore, previous studies have shown that MWCNTs optimized for operation within the X-band frequency range achieve superior performance when the material thickness is lower, with filler content below 4% [26]. These observations highlight the critical role of the interplay between material thickness and filler content in determining the electromagnetic absorption performance of such composites.

The observed electromagnetic response can be further interpreted by correlating the microstructural

characteristics with established structure–property relationships reported for microwave absorbers. Recent studies have shown that lattice strain, interfacial density, and conductive pathways play decisive roles in regulating dielectric loss and impedance behavior rather than magnetic loss alone. For instance, strain-engineered TMD systems exhibit enhanced polarization loss arising from modified electronic states and defect distributions, leading to improved microwave attenuation (Ref. [50]). Similarly, flexible polymer-based absorbers demonstrate that nanoscale interfacial architectures and phase distributions strongly influence dielectric relaxation and loss mechanisms (Ref. [51]), while MXene-based systems reveal that modulation of charge transport pathways and interlayer spacing critically governs microwave reflection and absorption behavior (Ref. [52]). In the present $SrFe_{12}O_{19}$/MWCNT composites, the CNT-induced interfacial regions and milling-induced defects predominantly enhance dielectric loss through interfacial polarization and conductive dissipation, whereas magnetic loss remains weak, consistent with the negligible μ'' values and the thickness-dependent RL trends observed in this study.

3.5 Permittivity and permeability analysis of $SrFe_{12}O_{19}$/MWCNTs nanocomposites

The real and imaginary components of permittivity and permeability are fundamental to understanding the mechanisms underlying microwave power absorption. The real permittivity (ε') and real permeability (μ') represent the material's ability to store electric and magnetic energy, respectively, while the imaginary components (ε'' and μ'') describe the material's energy dissipation capabilities. In this study, the complex permittivity and permeability were evaluated within the X-band frequency range (8–12 GHz) to analyze their contributions to microwave absorption.

The trend observed in the real part of permittivity (ε') from Fig. 6, which decreases from Sample S4 to S5 and then increases in S6, can be attributed to factors such as milling duration, thickness variations, and the incorporation of MWCNTs. The reduction in permittivity from S4 to S5 may result from the extended milling time, which enhances the dispersion of MWCNTs within the composite matrix, thereby influencing its dielectric properties. Yao et al. have noted that the presence of charge carriers at material interfaces significantly impacts permittivity, particularly at lower frequencies, due to the facilitation of interfacial polarization [53]. This observation aligns with studies indicating that the addition of conductive fillers like MWCNTs can induce negative permittivity effects in composites, especially within low-frequency ranges [54].

The increase in permittivity observed in Sample S6 could be attributed to the enhanced thickness of the composite, which likely facilitates a more favorable dielectric environment for polarization effects. The addition of inorganic fillers is known to improve the dielectric properties of composites, as evidenced by Zheng et al., who reported substantial increases in dielectric permittivity when barium titanate ($BaTiO_3$) particles were incorporated into poly(vinylidene fluoride) (PVDF) composites [55]. This suggests that the structural modifications and filler additions can lead to a complex interplay of dielectric behaviors across different frequency ranges.

The imaginary component of permittivity (ε''), representing dielectric loss, increases with the incorporation of MWCNTs, indicating their contribution to energy dissipation within the composite. This observation is consistent with Zhang et al., who emphasized the critical role of dielectric loss in microwave absorption performance, attributing it to multiple relaxation mechanisms that influence the composite's overall dielectric behavior [56]. Moreover, dielectric loss has been shown to decrease with increasing frequency, thereby enhancing the material's ability to absorb electromagnetic waves. This trend aligns with the findings of Gholipur et al., who reported that the energy of electromagnetic waves is often converted into thermal energy, effectively contributing to improved absorption characteristics [57].

Achieving robust dielectric properties in composites containing MWCNTs requires uniform dispersion of the nanotubes throughout the polymer matrix. Agglomeration of MWCNTs, particularly at higher concentrations, disrupts the formation of effective microcapacitors within the matrix, leading to an increased dielectric loss tangent. This disruption results in elevated energy dissipation and higher leakage currents due to the formation of pronounced conduction pathways. Zhao and Li have highlighted the importance of uniform MWCNT dispersion in optimizing the dielectric performance of poly(vinylidene fluoride-hexafluoropropylene) nanocomposites, noting that inadequate dispersion can significantly compromise the material's dielectric properties [58].

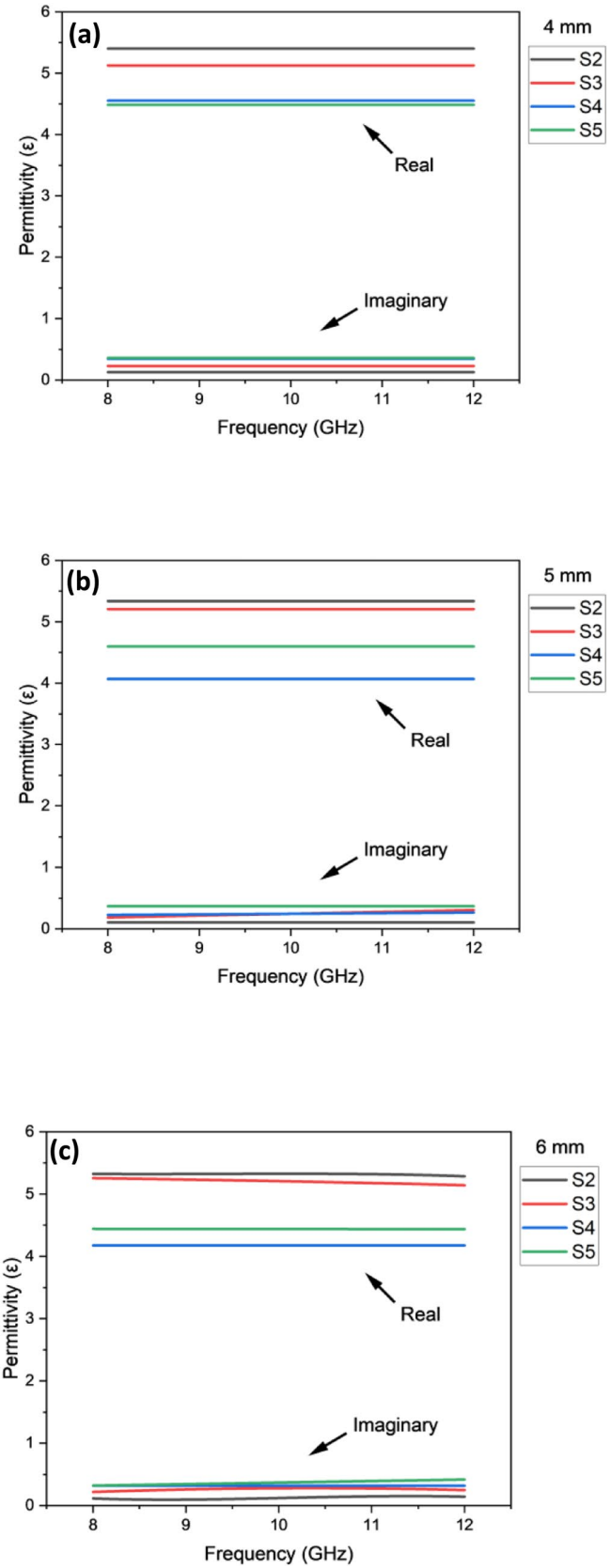

Fig. 6 Real and imaginary permittivity of **a** 4 mm, **b** 5 mm, and **c** 6 mm

Furthermore, Zheng et al. demonstrated that better dispersibility of MWCNTs within a high-density polyethylene/nitrile rubber matrix enhances charge accumulation and migration at the interface, which is critical for improving dielectric permittivity [55]. Conversely, when MWCNTs are agglomerated, the insulating barriers that typically prevent conductivity paths are compromised, leading to increased dielectric loss and leakage currents [55]. This aligns with findings from Uthaman et al., who reported that the mechanical properties of epoxy nanocomposites improved only up to a certain concentration of MWCNTs, beyond which the agglomeration negatively impacted performance [59].

Furthermore, the findings of Song et al. emphasize that the close proximity of MWCNTs is critical for forming effective polarized microcapacitors, which are integral to improving the dielectric properties of composite materials [60]. This indicates that achieving a uniform dispersion is not merely beneficial but essential for maximizing the dielectric characteristics of the composite materials. The detrimental effects of MWCNT agglomeration on dielectric loss tangent and leakage currents have also been corroborated by other studies, which suggest that maintaining a lower concentration of MWCNTs can mitigate these issues and enhance the overall performance of the composite [61].

Figure 7 presents the real (μ') and imaginary (μ'') components of magnetic permeability for samples with thicknesses of 4 mm, 5 mm, and 6 mm within the 8–12 GHz (X-band) frequency range. Across all samples (S2, S3, S4, S5, and S6), the real permeability (μ') remains relatively stable, with values near unity. This behavior indicates a weak magnetic response, consistent with the fact that MWCNTs are not strongly magnetic fillers. The findings align with the work of Zaric et al., who demonstrated the anisotropic magnetic susceptibilities of CNTs. While MWCNTs can exhibit a response to magnetic fields, this response is comparatively weak when measured against conventional magnetic materials. These characteristics show the limited contribution of MWCNTs to the magnetic permeability of the composites [62]. The authors demonstrated that the magnetic alignment of MWCNTs in solutions highlights their inherently weak magnetic characteristics, reaffirming that MWCNTs lack strong magnetic properties. Subtle variations in the real permeability (μ') observed among the samples may be attributed to minor magnetic interactions or the presence of trace impurities. However, the thickness and processing conditions of the composites do not significantly influence this aspect of their magnetic behavior.

The imaginary permeability (μ'') is significantly lower than the real permeability (μ'), indicating minimal magnetic losses in these samples. This behavior is consistent with the expected contribution of MWCNTs, which primarily affect the composite's electrical properties rather than its magnetic response. Consequently, the microwave absorption performance of these materials is predominantly governed by dielectric mechanisms, as evidenced by the permittivity variations discussed in Fig. 6. While increasing the sample thickness from 4 to 5 mm and then to 6 mm exerts a notable effect on the real and imaginary components of permittivity, its influence on the real and imaginary permeability is comparatively modest. Therefore, the improvements in microwave absorption observed in these composites can be largely attributed to their dielectric properties, with magnetic loss playing a relatively minor role in the overall performance of these MWCNT-based polymer systems.

Based on the combined magnetic, dielectric, and microstructural characterizations, the electromagnetic loss in the $SrFe_{12}O_{19}$/MWCNT composites is predominantly governed by dielectric mechanisms. The incorporation of MWCNTs enhances dielectric loss through interfacial polarization and conductive dissipation, as evidenced by the increased ε'' values, while magnetic loss remains minimal due to the near-unity μ' and negligible μ'' across the X-band. Additionally, the observed thickness-dependent RL behavior is strongly influenced by interference effects and impedance matching, with excessive thickness leading to peak shifting and reduced absorption efficiency.

4 Conclusion

This research aimed to thoroughly evaluate the electromagnetic wave absorption capabilities of composite nanomaterials formed by integrating $SrFe_{12}O_{19}$ with MWCNTs. These hybrid materials were investigated for their potential as advanced radar-absorbing materials with superior performance. A key focus of the study was the relationship between the thickness of the composite nanomaterials and their microwave absorption properties. Detailed analysis revealed that thickness values exceeding 3 mm did not result in significant improvements in RL, thereby deeming them less effective for radar absorption. The

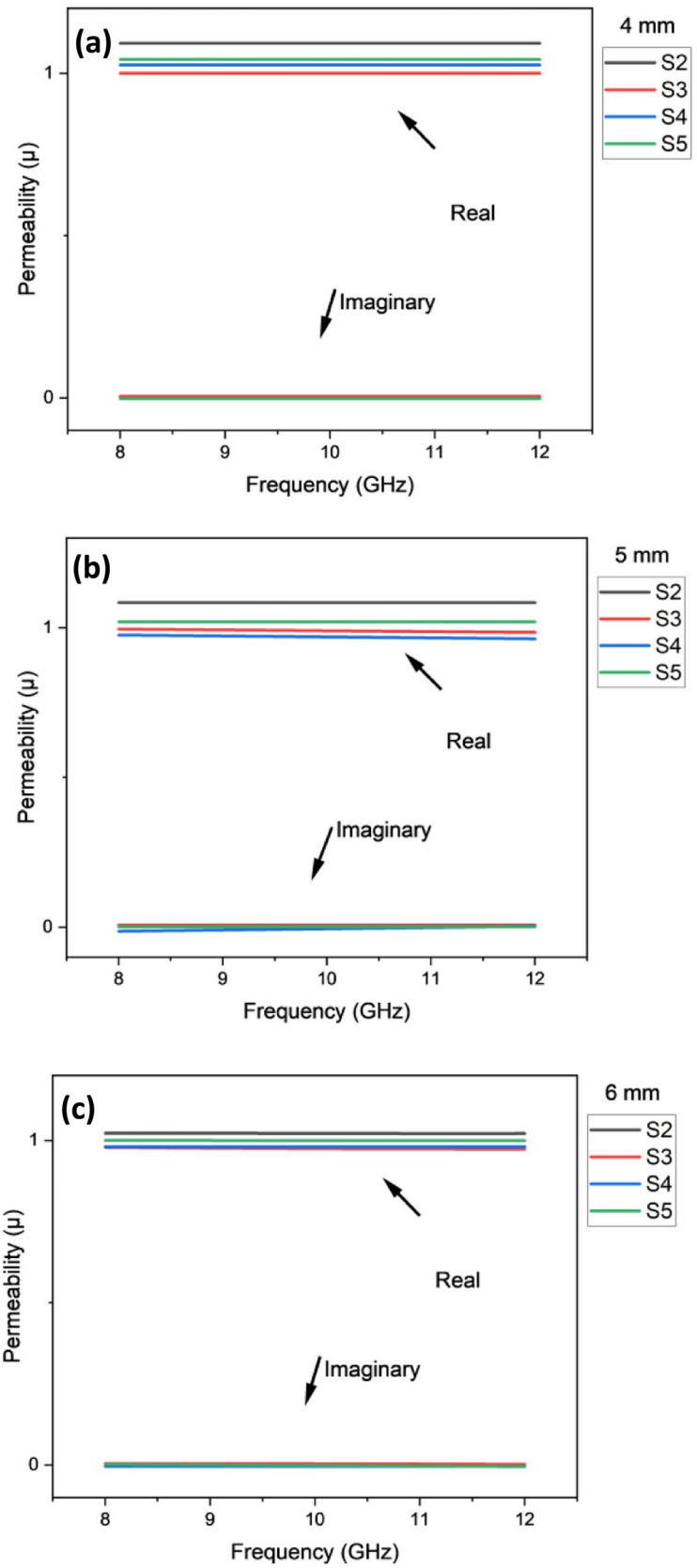

Fig. 7 Real and imaginary permeability of **a** 4 mm, **b** 5 mm, and **c** 6 mm

study identified an optimal thickness of 4 mm, which represented a critical balance between the material's absorption efficiency and its operational frequency range. This finding provides valuable insights for the strategic design and development of radar-absorbing materials capable of effectively interacting with incident electromagnetic waves. The research also explored the magnetic properties of the composite materials, including their saturation magnetization (M_s), retentivity (M_r), and coercivity (H_c). Samples hybridized with MWCNTs displayed significant variations in M_s and M_r, which were attributed to structural modifications induced by the presence of MWCNTs. The magnetic behavior of the composites was primarily governed by the $SrFe_{12}O_{19}$ component, with MWCNTs contributing unique characteristics that influenced the overall magnetic properties. These observations highlight the intricate interplay between the composite's constituents and their collective impact on magnetic performance. Future studies may focus on the synergistic optimization of MWCNT content and composite thickness to improve impedance matching and dielectric loss, as well as extending the investigation to other frequency bands beyond the X-band.

Acknowledgements

The authors extend their sincere appreciation to the MRUN Research Officer Grant Scheme (MROGS/2023/UPM-25) with Vot number 5539650 for the financial support and to Universiti Putra Malaysia (UPM), Malaysia, for facilitating the successful completion of this research project.

Author contributions

Ismayadi Ismail contributed toward supervision, conceptualization, methodology, validation, formal analysis, investigation, writing—original draft, and writing—review & editing. Rabaah Syahidah Azis contributed toward supervision, conceptualization, investigation, validation, and writing—review & editing. Puteri Noorzulaikha Mohd Badrizazli contributed toward methodology, validation, and investigation. Mohd Khairil Adzhar Mahmood contributed toward conceptualization, validation, and writing—review & editing.

Funding

Open access funding provided by The Ministry of Higher Education Malaysia and Universiti Putra Malaysia. This study was funded by MRUN Research Officer Grant Scheme, MROGS/2023/UPM-25

Data Availability

No datasets were generated or analyzed during the current study.

Declarations

Competing interests The authors declare no competing interests.

References

1. Y. Wang, Y. Guan, D. Liao, Y. He, S. Li, L. Zhou, C. Yu, Y. Chen, Y. Liu, H. Liu, Fabrication of cellulose nanofiber/reduced graphene oxide/nitrile rubber flexible films using Pickering emulsion technology for electromagnetic interference shielding and piezoresistive sensor. Macromol. Mater. Eng. (2021). https://doi.org/10.1002/mame.202100070

2. S. Kang, S. Qiao, Y. Cao, Z. Hu, J. Yu, Y. Wang, J. Zhu, Hyper-cross-linked polymers-derived porous tubular carbon nanofibers@TiO_2 toward a wide-band and lightweight microwave absorbent at a low loading content. ACS Appl. Mater. Interfaces **12**, 46455–46465 (2020). https://doi.org/10.1021/acsami.0c11839
3. Y. Yang, N. Wu, B. Li, W. Liu, F. Pan, Z. Zeng, J. Liu, Biomimetic porous MXene sediment-based hydrogel for high-performance and multifunctional electromagnetic interference shielding. ACS Nano **16**, 15042–15052 (2022). https://doi.org/10.1021/acsnano.2c06164
4. M. Fathi, M. Mehdipour, H. Shokrollahi, Investigation of microwave absorption properties of multi-layer nanostructure $BaFe_{12}O_{19}$/epoxy composites. J. Mater. Sci. Mater. Electron. **31**, 16918–16927 (2020). https://doi.org/10.1007/s10854-020-04247-0
5. Y. Zhao, Q. Wang, Y. Sun, S. Xuan, M. Li, A frequency selective surface loaded two-layer composite for tunable microwave absorption. Mater. Res. Express **9**, 066301 (2022). https://doi.org/10.1088/2053-1591/ac74a6
6. S. Wang, Y. Xu, R. Fu, H. Zhu, Q. Jiao, T. Feng, C. Feng, D. Shi, H. Li, Y. Zhao, Rational construction of hierarchically porous Fe–Co/N-doped carbon/rGO composites for broadband microwave absorption. Nano-Micro Lett. (2019). https://doi.org/10.1007/s40820-019-0307-8
7. M. Saura-Múzquiz, A.Z. Eikeland, M. Stingaciu, H.L. Andersen, C. Granados-Miralles, M. Avdeev, V. Luzin, M. Christensen, Elucidating the relationship between nanoparticle morphology, nuclear/magnetic texture and magnetic performance of sintered $SrFe_{12}O_{19}$ magnets. Nanoscale **12**, 9481–9494 (2020). https://doi.org/10.1039/d0nr01728k
8. E. Demir, S.E. Sünbül, K. Icin, Exploring the effects of annealing temperature on structural and magnetic properties of low-level neodymium-substituted strontium hexaferrite synthesized via combustion method. J. Mater. Mechat. A **4**, 446–458 (2023). https://doi.org/10.55546/jmm.1319818
9. P. Maltoni, T. Sarkar, G. Varvaro, G. Barucca, C.A. Иванов, D. Peddis, R. Mathieu, Towards bi-magnetic nanocomposites as permanent magnets through the optimization of the synthesis and magnetic properties of $SrFe_{12}O_{19}$ nanocrystallites. J. Phys. D **54**, 124004 (2021). https://doi.org/10.1088/1361-6463/abd20d
10. S. Katlakunta, S.S. Meena, S. Srinath, M. Bououdina, R. Sandhya, K. Praveena, Improved magnetic properties of Cr^{3+} doped $SrFe_{12}O_{19}$ synthesized via microwave hydrothermal route. Mater. Res. Bull. **63**, 58–66 (2015). https://doi.org/10.1016/j.materresbull.2014.11.043
11. S.E. Jacobo, P.G. Bercoff, C.A. Herme, L.A. Vives, Sr hexaferrite/Ni ferrite nanocomposites: magnetic behavior and microwave absorbing properties in the X-band. Mater. Chem. Phys. **157**, 124–129 (2015). https://doi.org/10.1016/j.matchemphys.2015.03.026
12. H. Liang, Y. Guo, S. Hui, Z. Hou, Z. Wang, H. Shen, H. Wu, Tailoring dielectric-magnetic synergy in bimetallic MOF-derived Cu/C@Fe_3O_4 for high-efficiency electromagnetic wave absorption. Carbon (2025). https://doi.org/10.1016/j.carbon.2025.120605
13. H. Liang, T. Hou, T. Liu, S. Hui, Z. Hou, Z. Wang, B. Shi, L. Zhang, H. Shen, H. Wu, Rare-Earth oxide-induced interfacial engineering for tailoring dielectric response in $NiCo_2O_4$/CeO_2 composites toward high-performance electromagnetic wave absorbers. Carbon (2026). https://doi.org/10.1016/j.carbon.2025.120922
14. L.A. Trusov, A.E. Sleptsova, J. Duan, E.A. Gorbachev, E.S. Kozlyakova, E.O. Anokhin, A.A. Елисеев, M.A. Karpov, A. Vasiliev, O. Brylev, П.Е. Казин, Glass-ceramic synthesis of Cr-substituted strontium hexaferrite nanoparticles with enhanced coercivity. Nanomaterials **11**, 924 (2021). https://doi.org/10.3390/nano11040924
15. S. Kolev, B. Georgieva, T. Koutzarova, K. Krezhov, C. Ghelev, D. Kovacheva, B. Vertruyen, R. Closset, L.M. Tran, M. Babij, A. Zaleski, Magnetic field influence on the microwave characteristics of composite samples based on polycrystalline Y-type hexaferrite. Polymers **14**, 4114 (2022). https://doi.org/10.3390/polym14194114
16. S.S. Satpute, S.R. Wadgane, S. Kadam, D.R. Mane, R.H. Kadam, Y^{3+} substituted Sr-hexaferrites: sol-gel synthesis, structural, magnetic and electrical characterization. Cerâmica **65**, 274–281 (2019). https://doi.org/10.1590/0366-69132019653742582
17. G.R. Gordani, A. Ghasemi, A. Saidi, High frequency electromagnetic reflection loss performance of substituted Sr-hexaferrite nanoparticles/SWCNTs/epoxy nanocomposite. J. Magn. Magn. Mater. **391**, 184–190 (2015). https://doi.org/10.1016/j.jmmm.2015.05.002
18. M. Rostami, M. Moradi, R.S. Alam, R. Mardani, Characterization of magnetic and microwave absorption properties of multi-walled carbon nanotubes/Mn-Cu-Zr substituted strontium hexaferrite nanocomposites. Mater. Res. Bull. **83**, 379–386 (2016). https://doi.org/10.1016/j.materresbull.2016.06.019
19. M. Asghari, A. Ghasemi, E. Paimozd, A. Morisako, Evaluation of microwave and magnetic properties of substituted $SrFe_{12}O_{19}$ and substituted $SrFe_{12}O_{19}$/multi-walled carbon nanotubes nanocomposites. Mater. Chem. Phys. **143**, 161–166 (2013). https://doi.org/10.1016/j.matchemphys.2013.08.045
20. A. Ghasemi, Remarkable influence of carbon nanotubes on microwave absorption characteristics of strontium ferrite/

CNT nanocomposites. J. Magn. Magn. Mater. **323**, 3133–3137 (2011). https://doi.org/10.1016/j.jmmm.2011.06.070

21. M.M.M. Zulkimi, R.S. Azis, I. Ismail, N. Mokhtar, M. Ertugrul, M.N. Hamidon, I.H. Hasan, Y.O. Yesilbag, F.N. Tuzluca, G. Ozturk, U.C. Hasar, Enhancing radar absorption performance of Sr-hexaferrite by hybridization with coiled carbon nanotubes via chemical vapour deposition method. Diam. Relat. Mater. **137**, 110118 (2023). https://doi.org/10.1016/j.diamond.2023.110118
22. N. Rosdi, R.S. Azis, I. Ismail, N. Mokhtar, M.M.M. Zulkimi, M.S. Mustaffa, Structural, microstructural, magnetic and electromagnetic absorption properties of spiraled multiwalled carbon nanotubes/barium hexaferrite (MWCNTs/$BaFe_{12}O_{19}$) hybrid. Sci. Rep. **11**, 15982 (2021). https://doi.org/10.1038/s41598-021-95332-9
23. P. Moodley, J. Loos, J.W. Niemantsverdriet, P.C. Thüne, Is there a correlation between catalyst particle size and CNT diameter? Carbon N Y **47**, 2002–2013 (2009). https://doi.org/10.1016/j.carbon.2009.03.046
24. V. Jourdain, C. Bichara, Current understanding of the growth of carbon nanotubes in catalytic chemical vapour deposition. Carbon **58**, 2–39 (2013). https://doi.org/10.1016/j.carbon.2013.02.046
25. B. Gu, C. Zhou, S. He, S. Moldovan, P.A. Chernavskii, V.V. Ordomsky, A.Y. Khodakov, Size and promoter effects on iron nanoparticles confined in carbon nanotubes and their catalytic performance in light olefin synthesis from syngas. Catal. Today **357**, 203–213 (2020). https://doi.org/10.1016/j.cattod.2019.05.054
26. R.C. Che, L.-M. Peng, X.F. Duan, Q. Chen, X.L. Liang, Microwave absorption enhancement and complex permittivity and permeability of Fe encapsulated within carbon nanotubes. Adv. Mater. **16**, 401–405 (2004). https://doi.org/10.1002/adma.200306460
27. M. Inagaki, Intensity ratios between 002 and 004 diffraction lines for various carbons. J. Appl. Crystallogr. **5**, 295–297 (1972). https://doi.org/10.1107/s0021889872009537
28. N. Cao, Y. Zhang, Study of reduced graphene oxide preparation by Hummers' method and related characterization. J. Nanomater. (2015). https://doi.org/10.1155/2015/168125
29. Y. Wu, Y. Wu, L. Li, Y. Wang, Effect of SDBS on crystallization behavior of pseudoboehmite. J. Phys. Chem. C **125**, 26039–26048 (2021). https://doi.org/10.1021/acs.jpcc.1c08074
30. X.F. Zhao, Y. Sun, T.J. Sun, J. Qiu, Preparation of a novel carbon nano-material studded iron granules from needle coke by arc method. Key Eng. Mater. **336–338**, 2186–2188 (2007). https://doi.org/10.4028/www.scientific.net/kem.336-338.2186
31. C. Suryanarayana, Mechanical alloying and milling. Prog. Mater. Sci. **46**, 1–184 (2001). https://doi.org/10.1016/S0079-6425(99)00010-9
32. L. Deng, M. Han, Microwave absorbing performances of multiwalled carbon nanotube composites with negative permeability. Appl. Phys. Lett. **91**, 2005–2008 (2007). https://doi.org/10.1063/1.2755875
33. A. Goldman, Handb. Mod. Ferromagn. Mater. (1999). https://doi.org/10.1007/978-1-4615-4917-8
34. E.C. Snelling, *Soft Ferrites: Properties and Applications*, 1st edn. (Iliffe, London, 1969)
35. J.R. Trelewicz, C.A. Schuh, The Hall–Petch breakdown in nanocrystalline metals: a crossover to glass-like deformation. Acta Mater. **55**, 5948–5958 (2007). https://doi.org/10.1016/j.actamat.2007.07.020
36. I. Ismail, M. Hashim, K.A. Matori, R. Alias, J. Hassan, The transition from paramagnetic to ferromagnetic states as influenced by evolving microstructure of $Ni_{0.5}Zn_{0.5}Fe_2O_4$. J. Supercond. Nov. Magn. **25**, 71–77 (2012). https://doi.org/10.1007/s10948-011-1201-x
37. N.D. Co, B.T.T. Thuy, N.T. Lưỡng, D.Q. Viet, L.Q. Cuong, ĐĐ Dũng, N.D. Quan, T.M. Danh, T. Pham, B.D. Tu, Characterization and microwave absorption properties of lead-free $Bi_{0.5}(Na_{0.80}K_{0.20})0.5TiO_3$ synthesized by sol-gel method. VNU J. Sci. Math. Phys. (2022). https://doi.org/10.25073/2588-1124/vnumap.4665
38. Y. Shi, Y. Yin, Y. Zhang, Y. Hu, W. Liu, Preparation and microwave absorption properties of C@Fe_3O_4 magnetic composite microspheres. Materials **12**, 2404 (2019). https://doi.org/10.3390/ma12152404
39. G. Dai, R. Deng, T. Zhang, Y. Yu, L. Song, Quantitative evaluation of loss capability for in situ conductive phase enhanced microwave absorption of high-entropy transition metal oxides. Adv. Funct. Mater. (2022). https://doi.org/10.1002/adfm.202205325
40. H. Zhang, B. Zhao, H. Xiang, F.-Z. Dai, Z. Zhang, Y. Zhou, Electromagnetic wave absorbing properties of Cr_2AlB_2 powders and the effect of high-temperature oxidation. J. Am. Ceram. Soc. **104**, 2213–2224 (2021). https://doi.org/10.1111/jace.17601
41. H. Luo, B. Ma, F. Chen, S. Zhang, Y. Xiong, Y. Cheng, R. Gong, Bimetallic oxalate rod-derived NiFe/Fe_3O_4@C composites with tunable magneto-dielectric properties for high-performance microwave absorption. J. Phys. Chem. C **125**, 24540–24549 (2021). https://doi.org/10.1021/acs.jpcc.1c04386
42. X. Guo, Z. Nie, Y. Feng, M. Jiang, Z. Zhao, X. Yang, R. Wang, S. Qi, In situ growth of CoNi alloy/N-doped hollow carbon foam for electromagnetic wave absorption. ACS

Appl. Nano Mater. **7**, 19427–19438 (2024). https://doi.org/10.1021/acsanm.4c03331

43. H. Cai, J. Guo, H. Hu, Y. Liu, M. Jia, H. Chen, G. Zhou, Carbon nanotube/$FeNi_3$ nanoparticle composites for electromagnetic wave absorption. ACS Appl. Nano Mater. **7**, 11302–11312 (2024). https://doi.org/10.1021/acsanm.4c00827
44. X. Dai, Q. Zhou, L. Dong, C. Zhang, X. Zhang, T. Ping, R. Lan, P. Yang, Y. Hou, Z. Bao, S. Yi, J. Rao, Y. Zhang, Nickel iron layered double hydroxide nanostructures composited with carbonyl iron powder for microwave absorption. ACS Appl. Nano Mater. **6**, 3472–3483 (2023). https://doi.org/10.1021/acsanm.2c05251
45. R.S. Yadav, A. Anju, T. Jamatia, I. Kuřitka, J. Vilčáková, P. Urbánek, M. Machovský, M. Masař, M. Urbánek, L. Kalina, J. Havlica, Superparamagnetic $ZnFe_2O_4$ nanoparticles-reduced graphene oxide-polyurethane resin based nanocomposites for electromagnetic interference shielding application. Nanomaterials **11**, 1112 (2021). https://doi.org/10.3390/nano11051112
46. M.S. Mustaffa, R.S. Azis, N.H. Abdullah, I. Ismail, I.R. Ibrahim, An investigation of microstructural, magnetic and microwave absorption properties of multi-walled carbon nanotubes/$Ni_{0.5}Zn_{0.5}Fe_2O_4$. Sci. Rep. **9**, 15523 (2019). https://doi.org/10.1038/s41598-019-52233-2
47. R. Liu, Z. An, B. Liao, J. Zhang, FeNi alloy and nickel ferrite codoped carbon hollow microspheres for high-efficiency microwave absorption. J. Mater. Chem. C **10**, 6085–6097 (2022). https://doi.org/10.1039/D2TC00135G
48. Z. Wu, K. Tian, T. Huang, W. Hu, F. Xie, J. Wang, M. Su, L. Li, Hierarchically porous carbons derived from biomasses with excellent microwave absorption performance. ACS Appl. Mater. Interfaces **10**, 11108–11115 (2018). https://doi.org/10.1021/acsami.7b17264
49. X. Shao, B. Dai, X. Zhang, Y. Ma, Synthesis and microwave absorption properties of magnetite nanoparticles. J. Nanosci. Nanotechnol. **12**, 1122–1127 (2012). https://doi.org/10.1166/jnn.2012.4275
50. J. Wen, Y. Liu, S. Hui, L. Deng, L. Zhang, X. Fan, Q. Chen, X. Liu, X. Li, N. Yan, H. Wu, Lattice compressive strain-controlled electromagnetic wave absorption in TMDs by plasma-assisted rapid annealing. Matter **8**, 102151 (2025). https://doi.org/10.1016/j.matt.2025.102151
51. Y. Liang, L. Deng, B. Luo, L. Zhang, K. Tao, X. Li, Q. Chen, H. Wu, Flexible, large area preparable phase change PVA/P(ILs-AM)/SSD films for electromagnetic wave absorption and infrared stealth. IScience **28**, 112366 (2025). https://doi.org/10.1016/j.isci.2025.112366
52. M. Han, D. Zhang, C.E. Shuck, B. McBride, T. Zhang, R (John). Wang, K. Shevchuk, Y. Gogotsi, Electrochemically modulated interaction of MXenes with microwaves. Nat. Nanotechnol. **18**, 373–379 (2023). https://doi.org/10.1038/s41565-022-01308-9
53. T. Yao, W. Zhou, G. Cao, W. Peng, J. Liu, X. Dong, X. Chen, Y. Zhang, Y. Chen, M. Yuan, Engineering of core@double-shell structured Zn@ZnO@PS particles in poly(vinylidene fluoride) composites towards significantly enhanced dielectric performances. J. Appl. Polym. Sci. (2023). https://doi.org/10.1002/app.53772
54. X. Zeng, G. Jiang, L. Zhu, C. Wang, M. Chen, R. Yu, Fe_3O_4 nanoflower-carbon nanotube composites for microwave shielding. ACS Appl. Nano Mater. **2**, 5475–5482 (2019). https://doi.org/10.1021/acsanm.9b01076
55. M.-S. Zheng, C. Zhang, Y. Yang, Z.-L. Xing, X. Chen, S.-L. Zhong, Z.-M. Dang, Improved dielectric properties of PVDF nanocomposites with core–shell structured $BaTiO_3$ @polyurethane nanoparticles. IET Nanodielectrics **3**, 94–98 (2020). https://doi.org/10.1049/iet-nde.2020.0015
56. Y. Zhang, H.-B. Zhang, X. Wu, Z. Deng, E. Zhou, Z.-Z. Yu, Nanolayered cobalt@carbon hybrids derived from metal-organic frameworks for microwave absorption. ACS Appl. Nano Mater. **2**, 2325–2335 (2019). https://doi.org/10.1021/acsanm.9b00226
57. R. Gholipur, K. Afrouzeh, Flexible PVA/Co ferrite/MWCNT/AC metacomposites: high conductivity and low percolation threshold. ACS Appl. Electron. Mater. **6**, 2609–2623 (2024). https://doi.org/10.1021/acsaelm.4c00202
58. X. Zhao, C. Li, Effects of multiwalled carbon nanotubes on phase transformation and dielectric properties in poly(vinylidene fluoride-hexafluoropropylene) nanocomposites. Mater. Trans. **60**, 1716–1721 (2019). https://doi.org/10.2320/matertrans.M2019040
59. A. Uthaman, H.M. Lal, C. Li, G. Xian, S. Thomas, Mechanical and water uptake properties of epoxy nanocomposites with surfactant-modified functionalized multiwalled carbon nanotubes. Nanomaterials **11**, 1234 (2021). https://doi.org/10.3390/nano11051234
60. X. Song, Q. Zhang, H. Wu, S. Guo, J. Qiu, Highly efficient dispersion of individual multiwalled carbon nanotubes by polylactide in high elastic state. Ind. Eng. Chem. Res. **62**, 5042–5050 (2023). https://doi.org/10.1021/acs.iecr.2c04609
61. G. Parameswarreddy, Y.R. Yadam, K. Arunachalam, R. Sarathi, H. Suematsu, Investigation on the enhancement of electromagnetic shielding with efficient use of short carbon

fiber in MWCNT-epoxy nanocomposites. Polym. Compos. **44**, 1522–1533 (2023). https://doi.org/10.1002/pc.27185

62. S. Zaric, G.N. Ostojic, J. Kono, J. Shaver, V.C. Moore, R.H. Hauge, R.E. Smalley, X. Wei, Estimation of magnetic susceptibility anisotropy of carbon nanotubes using magnetophotoluminescence. Nano Lett. **4**, 2219–2221 (2004). https://doi.org/10.1021/nl0486012